JOURNAL OF GEOPHYSICAL RESEARCH, VOL. 95, NO. A9, PAGES 15,073–15,089, SEPTEMBER 1, 1990

Space-Time Evolution of Whistler Mode Wave Growth in the Magnetosphere

C. R. CARLSON,[1] R. A. HELLIWELL, AND U. S. INAN

Space, Telecommunications, and Radioscience Laboratory, Stanford University, Stanford, California

A new model is developed to simulate the space-time evolution of a propagating coherent whistler mode wave pulse in the magnetosphere. The model is applied to the case of single frequency (2-6 kHz) wave pulses injected into the magnetosphere near $L \simeq 4$, using the VLF transmitting facility at Siple Station, Antarctica. The mechanism for growth is cyclotron resonance between the circularly polarized waves and the gyrating energetic electrons of the radiation belts. Application of this model reproduces observed exponential wave growth up to a saturated level. Additionally, the model predicts the observed initial linear increase in the output frequency versus time. This is the first time these features have been reproduced using applied wave intensities small enough to be consistent with satellite measurements. The center velocities of the electrons entering the wave pulse are selected in a way which maximizes the growth rate. The results show the importance of the transient aspects in the wave growth process. The growth established as the wave propagates toward the geomagnetic equator results in a spatially advancing wave phase structure due mainly to the geomagnetic inhomogeneity. Through the feedback of this radiation upon other electrons, conditions are established which result in a linearly increasing output frequency with time.

1. INTRODUCTION

The main focus of this paper is the modeling and simulation of the growth of ducted, single frequency whistler mode waves through cyclotron resonance with radiation belt electrons. The growth of single frequency waves is commonly seen to occur on signals from ground based, VLF (very low frequency) transmitters, including signals from the Stanford University VLF transmitter at Siple Station, Antarctica ($L \simeq 4$) [*Helliwell and Katsufrakis*, 1974, 1978]. The Siple transmitter and the geomagnetically conjugate receiving station at Roberval, Quebec (now at Lake Mistissini, Quebec), are used to investigate a broad range of topics. While this paper is concerned with single frequency waves, the results can be applied to signals of slowly varying frequency [*Helliwell*, 1970; *Carlson et al.*, 1985] and even to broadband 'noise-like' signals [*Helliwell et al.*, 1986].

Two characteristic measures of wave growth are growth rate and saturation level. The growth itself can be somewhat irregular but in many cases is exponential, with growth rates between 25 dB/s and 250 dB/s, and 20-35 dB of total growth to saturation [*Stiles and Helliwell*, 1977]. Satellite data on the unamplified signal strength are limited and no in situ measurement of the amplitude of a ducted signal has yet been made. Satellite based field strength measurements of nonducted Siple signals place the input field strength at $L \simeq 4.5$ between 0.01 pT and 0.3 pT [*Inan et al.*, 1977; *Rastani et al.*, 1985]. The actual field strength necessary for wave growth within a duct is of interest since there is a power threshold below which temporal wave growth is not observed [*Helliwell et al.*, 1980]. Since temporal growth of a coherent signal can be reduced when a noisy interfering signal is added [*Raghuram et al.*, 1977], it could be that a critical signal-to-noise ratio must be exceeded before temporal wave growth is possible. Another possible explanation is related to the nonlinear dynamics of the wave particle interaction. Several theoretical works have assumed a priori that only electrons trapped in the wave potential well contribute significantly to the wave growth [*Das and Kulkarni*, 1975; *Dowden et al.*, 1978; *Nunn*, 1971, 1974, 1984; *Roux and Pellat*, 1978; *Sudan and Ott*, 1971]. The trapping region is confined and centered on the geomagnetic equator by the inhomogeneity. If a minimum trapping region length were required for wave growth to occur, then this would imply a threshold mechanism since the physical length of the trapping region increases with increasing wave intensity. However, the satellite based field strength measurements and ground based experiments suggest that trapping may not be required for wave growth to occur. In one threshold study, *Helliwell et al.* [1980] found that as little as 1 W of radiated power from the Siple Station VLF transmitter could stimulate growth and triggering. Computer simulations also indicate that both trapped and untrapped electrons can contribute significantly to wave growth [*Omura and Matsumoto*, 1982]. A possible saturation mechanism related to the onset of trapping [*Helliwell and Inan*, 1982] results in a saturation intensity consistent with both the total growth and applied field measurements.

Experimental measurements of whistler mode wave growth have produced data on both the amplitude and phase evolution of a received signal. While the spectral characteristics of these signals have been known for many years, most studies have examined only signal amplitudes versus frequency and time and have not considered the signal's phase. Recent work has begun to include phase analysis [*Paschal*, 1988; *Paschal and Helliwell*, 1984; *Dowden et al.*, 1978; *Rietveld et al.*, 1978; *Rietveld*, 1980]. Phase measurements of signals from VLF transmitters [*Dowden et al.*,

[1]Presently at CAE-Link Corp., Link Flight Simulation Division, Sunnyvale, California.

Paper number 90JA00889.
0148-0227/90/90JA-00889$05.00

1978; *Paschal*, 1988; *Paschal and Helliwell*, 1984] show that pulses with temporal growth exhibit a relative phase advance with time and thus a positive frequency offset from the transmitted signal, often starting at the very beginning of the pulse.

One of the pulses analyzed by *Paschal and Helliwell* [1984] is reproduced in Figure 1 which shows the dynamic frequency-time spectrum, amplitude in a narrow band centered on the carrier, and phase versus time relative to the carrier. In addition to an exponential wave growth (36 dB/s) up to a saturated level, Figure 1 shows an initial frequency offset (1.1 Hz), advance in phase during wave growth, and the triggering of a rising emission. The instantaneous frequency relative to the applied frequency is plotted in Figure 2 and indicates that prior to triggering, the phase advance versus time is nearly parabolic since the frequency increase rate is nearly constant at ~ 10 Hz/s. At the point of triggering, the rate of frequency increase jumps up to the rising emission df/dt of ~ 700 Hz/s. Measurements made of a few more pulses which showed exponential wave growth accompanied by a nearly constant rate of frequency increase gave pre-triggering rates of frequency increase as high as 60 Hz/s.

Cyclotron resonance as a mechanism for whistler mode wave growth was first suggested by *Brice* [1963] and *Dungey* [1963] and has been the basis for most theoretical treatments and simulations which followed. A review of the early ideas is given by *Helliwell* [1965] and a review of attempts to understand coherent effects in whistler mode wave-particle interactions prior to 1979 is given by *Matsumoto* [1979]. *Helliwell* [1967] proposed a phenomenological theory for the growth and triggering of coherent whistler mode waves which utilized both nonlinear currents and the inhomogeneity. Helliwell's theory included a nonlinear saturation mechanism and linked the frequency evolution to the inhomogeneity of the geomagnetic field. Figure 3 summarizes the role

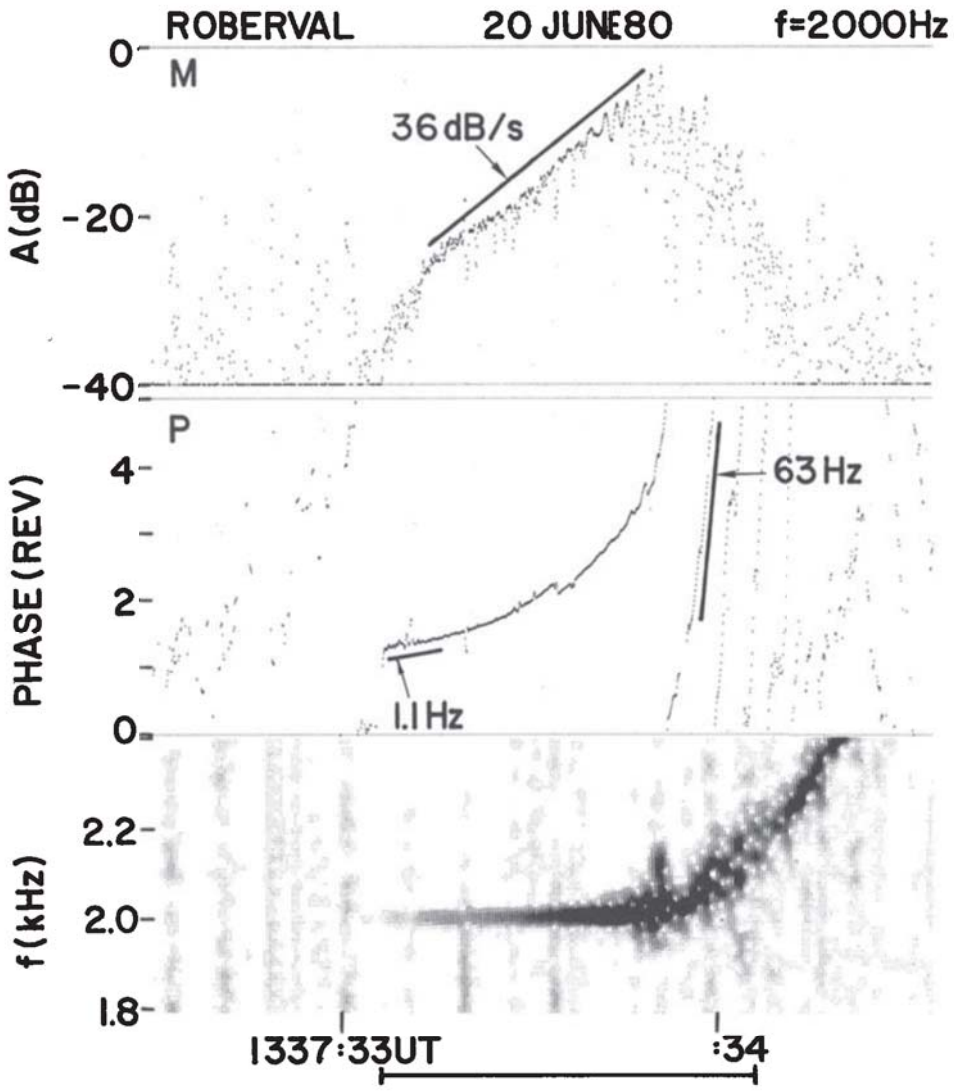

Fig. 1. Displays of a 1 second, 2 kHz Siple pulse received at Roberval (from *Paschal and Helliwell* [1984]). The spectrogram (bottom panel) shows a triggered rising emission. The magnitude plot (top panel) indicates a 36 dB/s growth rate up to a saturated level after $\sim$ 20 dB of total growth. The phase relative to the transmitted phase (middle panel) shows an initial frequency offset of 1.1 Hz from the transmitted signal. The phase advance with time, prior to triggering, is nearly parabolic indicating a linear increase in frequency with time.

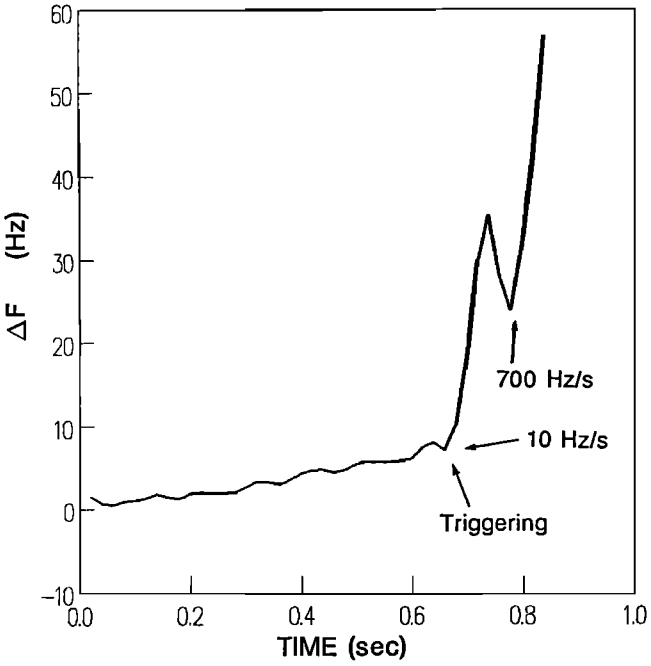

Fig. 2. Frequency versus time for the pulse in Figure 1 calculated from the slope of the phase curve. Prior to triggering, the frequency increases nearly linearly with time at ~ 10 Hz/s. At the point of triggering, the rate of frequency increase jumps up to the rising emission df/dt of ~ 700 Hz/s.

of the inhomogeneity, indicating that coherent VLF waves propagating along the geomagnetic field will interact significantly with the energetic electrons around the geomagnetic equator if the signal is constant in frequency. However, if the wave frequency is increasing or decreasing with time, then the interaction region will be located downstream or upstream of the geomagnetic equator, respectively. Second order resonance, described in the next section, is the mechanism governing this relationship between a signal's df/dt and the interaction region location. Helliwell's theory has proved to be a useful tool for interpreting experimental results [*Carlson et al.*, 1985; *Dowden*, 1971a,b; *Dysthe*, 1971; *Helliwell*, 1970; *Helliwell et al.*, 1986a,b].

Most other studies of gyroresonance interaction were performed within the framework of a linear or quasilinear approach (for reviews see *Liemohn* [1974], or *Matsumoto* [1979]) with the most notable being the work by *Kennel and Petschek* [1966]. However, there is general agreement that the emission triggering process involves both the nonlinearity and the inhomogeneity [*Matsumoto*, 1979]. Several theoretical works and models of gyroresonance interaction have specifically included the geomagnetic inhomogeneity [*Bell*, 1984, 1986; *Bell and Inan*, 1981; *Carlson et al.*, 1985; *Das and Kulkarni*, 1975; *Dowden*, 1971a,b; *Dowden et al.*, 1978; *Dysthe*, 1971; *Helliwell*, 1967, 1970; *Helliwell and Inan*, 1982; *Helliwell et al.*, 1986a,b; *Karpman et al.*, 1974a,b, 1975; *Matthews et al.*, 1984; *Matsumoto and Omura*, 1981, 1983; *Murdoch*, 1983; *Neubert et al.*, 1987; *Nunn*, 1971, 1974, 1984; *Omura*, 1985; *Rathmann et al.*, 1978; *Roux and Pellat*, 1978; *Sudan and Ott*, 1971; *Vomvoridis and Denavit*, 1979, 1980; *Vomvoridis et al.*, 1982]. In order to gain more insight or test theories, a few researchers have turned to computer simulation. Some whistler mode wave growth simulation efforts include, in some form, the geomagnetic inhomogeneity [*Omura*, 1985; *Omura and Matsumoto*, 1982; *Rathmann et al.*, 1978; *Vomvoridis and Denavit*, 1980].

While most treatments attempt to explain the overall frequency characteristics of amplification and emissions, *Paschal and Helliwell* [1984] noted that only those by *Nunn* [1974], *Dowden et al.* [1978], and *Helliwell and Inan* [1982] discuss the phase behavior. Each of these results appear to be consistent with the general phase advance during the growth of a transmitted pulse. However, both Nunn and Dowden require unsubstantiated loss mechanisms for saturation. While Nunn and Helliwell and Inan discuss the phase evolution in detail, Nunn produces an initial phase decrease before phase advance, and Helliwell and Inan produce an initial phase advance followed by phase retardation. The data, on the other hand, exhibit a generally advancing phase during wave growth and prior to the termination of the applied pulse.

The primary objective of the simulation and modeling presented here is to identify the aspects of the wave-particle interaction that lead to the features described above and shown in Figure 1. These features include exponential wave growth, saturation, and a linear increase in frequency with time, all resulting from applied wave intensities of less than 0.3 pT.

The wave growth model developed in this paper is quite similar to the feedback model of *Helliwell and Crystal* [1973] and to the long-time-scale algorithm [*Omura and Matsumoto*, 1982; *Rathmann et al.*, 1978]. Unique to this model are a few approximations including some afforded by using an applied wave frequency half that of the equatorial electron gyrofrequency. Also unique to this model is the use of a time varying energetic electron distribution designed to compensate for the necessity to artificially limit the distribution. Previous simulation efforts have limited the energetic electrons by including mono velocity electrons, a Maxwellian distribution of electrons, or only trapped electrons. One problem with mono velocity or Maxwellian distributions is that their center velocities have been fixed, causing the wave

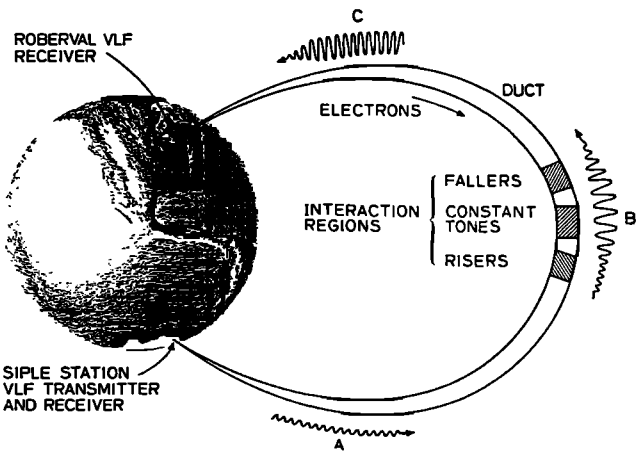

Fig. 3. Sketch of ducted VLF propagation from Siple Station, Antactica, and Roberval, Quebec (from *Helliwell* [1986]). As suggested by *Helliwell* [1967] the interaction region is centered on the equator for constant frequency signals (represented by the sketched waveform), and upstream or downstream of the equator for falling or rising frequency signals, respectively.

to drift out of resonance with the electrons as the frequency of the wave changes. An ideal solution would include a range of electrons so broad that the wave would always resonate with electrons without "seeing" the edges of the distribution. However, for a short wave pulse (0.25 s) propagating through the equatorial region (2000 km), the range of electron velocities might have to be greater than 10% of the center velocity of the distribution (in terms of the electron velocity component parallel to the earth's magnetic field). The computation time required makes such a simulation prohibitive. As a compromise, the center velocity of the distribution in our model varies in accordance with second order resonance theory in order to stay in resonance with the wave.

The next section reviews the basic theory of whistler mode wave propagation, wave-particle interactions, and wave growth. Section 3 develops the model used in section 4 to simulate whistler mode wave growth. And finally, in section 5, the main results are summarized. A more detailed development of the work presented in this paper can be found in *Carlson* [1987] including the computer program source code used for the simulations.

2. THEORY

In the following, a model of the inner magnetosphere is developed upon which group velocity, phase velocity, wave number, gyrofrequency, plasma frequency, and other parameters are based. These parameters are used in the equations of motion, to obtain electron trajectories, transverse currents, and stimulated whistler mode radiation. The numerical techniques employed are also discussed.

Whistler Mode Wave Propagation

The model of the magnetospheric medium is chosen to represent a typical ducted path for signals from the Siple Station transmitter. The waves will be assumed to be longitudinally propagating with the wave vector, k, parallel to the static magnetic field $\mathbf{B_0}$. All wave and medium parameters are assumed to be uniform over any plane perpendicular to the static magnetic field (i.e. one-dimensional). The strength of the static magnetic field versus position z, along the field is taken to be the same as a dipole geomagnetic field having an equatorial radius four times the earths' radius ($L = 4$). While a one-dimensional, z dependent static magnetic field does not satisfy Maxwell's equation $\nabla \cdot \mathbf{B} = 0$, the effects of this approximation upon wave propagation and electron motion can be neglected. The z dependence of the cold plasma density is calculated using a 'DE-1' diffusive equilibrium model [*Angerami and Thomas*, 1964] with an equatorial number density of $N_{eq} = 400$ el/cm^3.

For ducted whistler mode propagation, the magnetospheric medium is believed to vary so slowly that the WKB approximation [*Budden*, 1961] can be used. Accordingly, in the equations for wave propagation employed here, we assume that the WKB approximation is valid. Even for the wave growth calculations, when the wave frequency becomes a function of space and time, the wave is assumed to propagate as a single frequency wave. Expressions for the wave number (assuming $f_P >> f_H$), phase velocity, and group velocity, are respectively

$$k = \frac{2\pi f_P}{c}\sqrt{\frac{f}{f_H - f}} \tag{1}$$

$$v_p = \frac{2\pi f}{k} \tag{2}$$

$$v_g = 2v_p\left(1 - f/f_H\right) \tag{3}$$

where f, f_H, and f_P are the wave, electron gyrofrequency and plasma frequency respectively, and c is the free-space velocity of light. While k, v_p, and v_g all depend upon z, the (z) has been dropped for convenience in the above expressions and in many of the following expressions. The wave field components are also functions of z. It is assumed that the wave energy is confined to the duct and is uniformly distributed over any cross-section of the duct. For a dipole field, the cross-sectional area of a field aligned duct is inversely proportional to the dipole field intensity. For this model, the wave intensity associated with a wave group, in the absence of wave growth or damping, is related to the equatorial wave intensity of the same group by [*Inan et al.*, 1982]

$$B_w = B_{w\,eq}\sqrt{\frac{k f_H}{k_{eq} f_{H\,eq}}} \tag{4}$$

where the 'eq' subscripts denote equatorial values. While this factor is included, its effect is neglegible for the conditions encountered in this paper.

Energetic Electron Distribution Function

The magnitude of currents and stimulated fields calculated from electron trajectories depend upon the number of energetic electrons involved in the interaction and on the distribution of these electrons in velocity and configuration space. Although there are several ways to represent this information [*Roederer*, 1970], the velocity space distribution function $f(v,\alpha)$ is well suited to wave-particle interaction studies.

The velocity space distribution function $f(v,\alpha)$ has dimensions of m^{-6} s^3 ster^{-1} so that the number density of electrons is determined by integrating over velocity space. The velocity space volume element, given in terms of velocity, pitch angle, and gyrophase, is $v^2 \sin\alpha dv d\alpha d\theta$. Since the distribution function is assumed to be uniform in gyrophase, integration over θ yields 2π. Thus, the number density of electrons at any point in space is

$$N(z) = 2\pi \int_{\alpha}\int_{v} f(v,\alpha) v^2 \sin\alpha \; dv d\alpha \quad \left(\mathrm{m}^{-3}\right) \tag{5}$$

Choosing the limits of integration in (5) gives the number density within the selected region of velocity space.

It is convenient to work only with the equatorial distribution function $f(v,\alpha_{eq})$ rather than having to know $f(v,\alpha)$ at every point along the field line. An adiabatic transformation of (5) involves only $\sin\alpha d\alpha$ and gives

$$N(z) = \frac{\pi f_H}{\sqrt{f_{H\,eq}}} \int_{\alpha_{eq}}\int_{v} f(v,\alpha_{eq}) \cdot \frac{v^2 \sin(2\alpha_{eq})}{\sqrt{f_{H\,eq} - f_H \sin^2\alpha_{eq}}} \, dv d\alpha_{eq} \tag{6}$$

The model for $f(v,\alpha_{eq})$ used in this paper is [*Inan*, 1977]

$$f(v,\alpha_{eq}) = A v^{-n} g(\alpha_{eq}) \tag{7}$$

where A and n are constants and $g(\alpha_{eq})$ represents the pitch

angle dependence. Observed distributions are conventionally described using the differential energy spectrum which has units $m^{-2}\ s^{-1}\ ster^{-1}\ keV^{-1}$. The constant A is related to the differential energy spectrum Φ_{E_0} of electrons at a given energy E_0 (keV) and with $\alpha = 90^\circ$ by

$$A = \Phi_{E_0}\left(\frac{m^2}{mc^2}\right)\left(\frac{{\gamma_0}^5}{{\gamma_0}^2 - 1}\right){E_0}^{n/2} \qquad (8)$$

where mc^2 is the rest energy of the electron and $\gamma_0 = (1 - v^2/c^2)^{-1/2}$ is the relativistic constant associated with E_0 [*Chang*, 1983; *Chang and Inan*, 1983].

Dynamics of Near Resonant Particles

The magnetically trapped particles which make up the hot plasma, gyrate about the geomagnetic field while bouncing between conjugate mirror points. Compared to the size of the wave-particle interaction region, any cross-field drifts are believed to be insignificant and are neglected. Thus, the electron motion can be described by simple gyro motion centered on a single field line. For more details of charged particle motion see *Hess* [1968], *Roederer* [1970], and *Artsimovich and Lukyanov* [1980].

A framework useful for describing electron motion is defined in Figure 4 in which the electron velocity vector v is expressed in a cylindrical coordinate system, with velocity components perpendicular, $v_\perp$, and parallel, $v_\parallel$, to the geomagnetic field $\mathbf{B}_0$, gyrophase angle θ, and pitch angle α.

The whistler mode wave propagating in the same direction as the geomagnetic field is right-hand circularly polarized while counterstreaming electrons trace out left-handed helices. Cyclotron resonance occurs when the Doppler-shifted wave frequency seen by an electron matches the electron gyrofrequency. In the vicinity of this resonance, an electron sees a slowly varying or stationary wave field. Assuming longitudinal propagation, the cyclotron resonance condition is

$$v_\parallel \simeq v_R = \frac{2\pi}{k}\left(\frac{f_H}{\gamma} - f\right) \qquad (9)$$

where γ is the relativistic constant and v_R is the resonance velocity. For the cases considered here, $\gamma \simeq 1$ since the energies of resonant electrons are typically $\lesssim 50$ keV.

Figure 5 defines some angular relationships, at any point in space, useful for describing cyclotron resonant wave-particle interactions. All angles are positive in the direction of wave rotation. $\mathbf{B}_{in}$ and $\mathbf{E}_{in}$ represent the components of the single frequency, externally applied field which has propagated into the interaction region. $\mathbf{B}_{in}$ is governed only by cold plasma propagation making it useful as a reference wave structure. The total wave field, $\mathbf{B}_w$ and $\mathbf{E}_w$, makes an angle ψ with the reference field. Each electrons' cyclotron phase ϕ is measured from $-\mathbf{B}_w$.

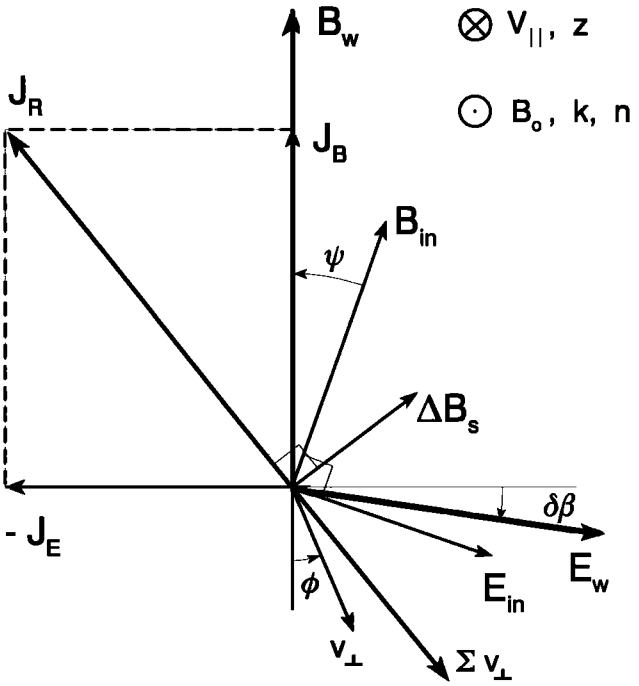

Fig. 5. Sketch defining the angular relationships, at any point in space, between the waves, electrons, and currents. $\mathbf{B}_{in}$ and $\mathbf{E}_{in}$ are the applied wave field. $\mathbf{B}_w$ and $\mathbf{E}_w$ are the total wave field vectors. Each electrons' cyclotron phase ϕ is measured from $-\mathbf{B}_w$. Associated with the net perpendicular velocity of a group of electrons $\Sigma \mathbf{v}_\perp$, is the resonant current $\mathbf{J}_R$. $\mathbf{J}_B$ and $\mathbf{J}_E$ are the components of $\mathbf{J}_R$ parallel and perpendicular to $\mathbf{B}_w$, respectively. $\Delta\mathbf{B}_s$ is the sheet current radiation associated with, and orthogonal to, $\mathbf{J}_R$. The angle between $\mathbf{B}_w$ and $\mathbf{E}_w$ deviates from 90° by $\delta\beta$ and is related to the instantaneous growth rate.

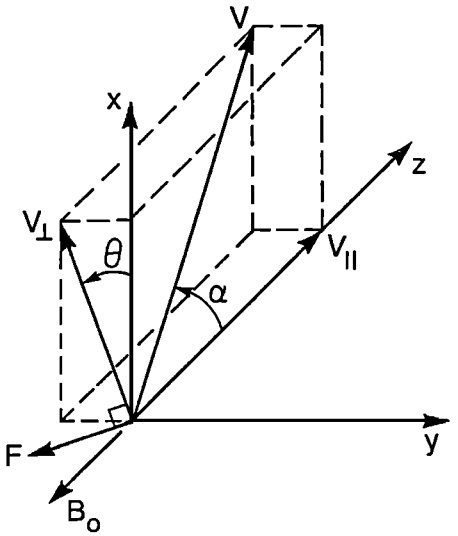

Fig. 4. Sketch showing the relationship of the electrons' velocity vector to the geomagnetic field $\mathbf{B}_0$. Defined are the total velocity v, pitch angle α, parallel velocity $v_\parallel$, perpendicular velocity $v_\perp$, and gyrophase θ. Due to the $\mathbf{v}_\perp \times \mathbf{B}_0$ force $\mathbf{F}$, the electron gyrates about the geomagnetic field at the gyrofrequency $f_H = (2\pi)^{-1} d\theta/dt$.

In the interaction model developed by *Helliwell* [1967] the length of the wave-particle interaction region, for a fixed frequency wave, maximizes at the equator. To visualize this, assume adiabatic electron motion. When $d\phi/dt = 0$, the resonance condition (9) is satisfied and the wave and the electron are said to be in first order resonance. The effective length of resonance (i.e. the length of the region over which ϕ varies by π [*Helliwell*, 1970]) maximizes when $d^2\phi/dt^2 = 0$, a condition known as 'second order resonance'. The second order resonance location depends upon the local change in

wave frequency with time, $\partial f/\partial t$. In other words, second order resonance occurs if the variation of the electron parallel velocity $v_{\|}$ along the electron orbit is matched by the variation of v_R. For constant frequency signals, second order resonance occurs with electrons resonant at the magnetic equator. Electrons with $v_{\|eq} > v_{Req}$ experience first order resonance on either side of the magnetic equator while, for electrons with $v_{\|eq} < v_{Req}$, (9) is not satisfied anywhere. A more general description of second order resonance is given by *Helliwell*, [1970] or *Carlson et al.*, [1985].

Changes in wave amplitude or frequency are a direct result of Lorentz wave forces altering the particle distribution, resulting in a net particle current and hence radiation. The equations of motion for an electron with a center of gyration fixed to a single field line and including the Lorentz wave force terms are

$$\frac{dv_{\|}}{dt} = \frac{eB_w}{m} v_{\perp} \sin\phi - \frac{{v_{\perp}}^2}{2f_H} \frac{\partial f_H}{\partial z} \tag{10a}$$

$$\frac{dv_{\perp}}{dt} = -\frac{eB_w}{m}\left(v_{\|} + v_p\right)\sin\phi + \frac{v_{\perp} v_{\|}}{2f_H} \frac{\partial f_H}{\partial z} \tag{10b}$$

$$\frac{d\phi}{dt} = k\left(v_R - v_{\|}\right) - \frac{eB_w}{m}\left(v_{\|} + v_p\right)\frac{\cos\phi}{v_{\perp}} - \frac{d\psi}{dt} \tag{10c}$$

$$\frac{dz}{dt} = v_{\|} \tag{10d}$$

Except for the addition of $d\psi/dt$, these equations are similar to those derived elsewhere [*Dysthe*, 1971; *Inan*, 1977]. In order to compute electron trajectories, these equations must be integrated. The method used in this paper is a fourth-order predictor-corrector method developed by *Ralston* [1978]. This method, employed by *Inan* [1977], was chosen to have both reasonably small error and numerical stability.

By including the $d\psi/dt$ term, the equations of motion become valid for a time dependent wave structure so long as the wave frequency and wave number change slowly. In such a case, time and position dependent offsets $\Delta\omega$, Δk, and Δv_p arise relative to the reference or unperturbed quantities ω, k, and v_p. The phase velocity offset is neglected since it appears only as a small correction to the perpendicular Lorentz force terms in equations (10b) and (10c) or equivalently,

$$v_{\|} + v_p + \Delta v_p \simeq v_{\|} + v_p \tag{11}$$

The expression for $d\phi/dt$, including $\Delta\omega$ and Δk is

$$\frac{d\phi}{dt} = \omega_H - \left(\omega + \Delta\omega\right) - v_{\|}\left(k + \Delta k\right) - \frac{eB_w}{m}\left(v_{\|} + v_p\right)\frac{\cos\phi}{v_{\perp}} \tag{12}$$

which is exactly equation (10c) since

$$\frac{d\psi}{dt} = \frac{\partial\psi}{\partial t} + \frac{\partial\psi}{\partial z}\frac{dz}{dt} = \Delta\omega + \Delta k v_{\|} \tag{13}$$

The previous discussion neglects the effect of Δv_p upon wave propagation since it is assumed that all wave energy propagates at the reference phase and group velocities. However, given two waves at slightly different frequencies, an observer moving at the phase velocity of one of the waves experiences a rotating wave field. To derive a general expression for this phase rotation, start with the following WKB description of the wave phase

$$\xi(\omega, z, t) = \int_0^t \omega dt - \int_0^z k dz \tag{14}$$

Converting this into the frame of the phase velocity of a reference wave gives

$$\xi_{ref}(\omega, z) = \xi(\omega, z, t)\Big|_{\frac{dz}{dt} = v_p(\omega_{ref}, z)} = \int_0^z \left(\frac{\omega}{v_p} - k\right) dz \tag{15}$$

Taking the derivative of equation (15) with respect to ω gives the relative phase delay which, when multiplied by the frequency separation, approximately gives the amount of accumulated phase rotation of the second wave that the observer would record as a function of position and frequency separation,

$$\Delta f \frac{d\xi_{ref}}{d\omega} = \Delta f \int_0^z \left(\frac{1}{v_p} - \frac{1}{v_g}\right) dz \ \text{(cycles)} \tag{16}$$

Figure 6 shows the relative phase delay $d\xi_{ref}/d\omega$ as a function of the normalized frequency and parametric in N_{eq} for waves which have propagated across the interaction region (taken to be from 250 to −250 km at $L = 4$). The relative phase delay is converted into a phase shift with units of degrees/Hertz in order to make it easier to apply. For example, if $f/f_{Heq} = 0.375$, $N_{eq} = 400$ el/cm^3, and the frequency separation is 10 Hz, the observed relative phase shift would be $\sim 33°$. Thus, to minimize the error associated with propagating all energy at frequency-independent group and phase velocities, the applied frequency should be either near the equatorial half gyrofrequency, where $v_p = v_g$, or the simulations should be limited to cases of small frequency deviation. In this paper, $f/f_{Heq} = 0.5$ for the applied wave.

Wave Growth

The equations of motion (10) show that the Lorentz forces can accelerate the electrons and can also alter the electron's

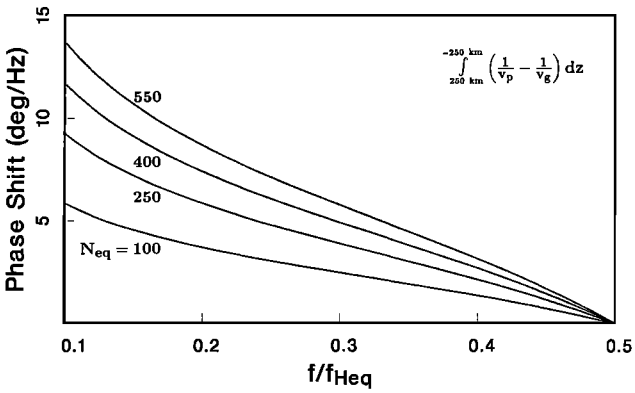

Fig. 6. The relative phase shift for two waves, 1 Hz apart, after propagating from −250 to 250 km, plotted versus normalized wave frequency and parametric in equatorial electron density N_{eq}. This is the total shift in phase of the higher frequency wave, relative to the lower frequency wave, as measured by an observer moving at the phase velocity of the lower frequency wave.

instantaneous gyrofrequency, depending upon the cyclotron phase ϕ. Changes in particle velocity, and hence energy, are due exclusively to the wave electric field while the changes in α and ϕ are due to both $\mathbf{B}_w$ and $\mathbf{E}_w$ [*Inan*, 1977]. For this reason, $\mathbf{B}_w$ and $\mathbf{E}_w$ work together to set up conditions for wave growth and damping. The $\mathbf{v}\times\mathbf{B}_w$ force tries to pull all of the electrons into a position such that the $\mathbf{v}_\perp$'s are antiparallel to $\mathbf{B}_w$. Since $\mathbf{B}_w$ can not do any work on the electrons, this is accomplished by exchanging parallel and perpendicular electron kinetic energies. This amounts to translating the electron helices in space with respect to their adiabatic helices so that their cyclotron phases tend to become bunched rather than uniformly distributed. This condition is refered to as phase bunched. Phased bunched electrons constitute a transverse right-hand polarized current $\mathbf{J}_R$, which radiates, and thus alters, the whistler mode wave frequency and amplitude. For small pitch angle electrons, the bunching effect of $\mathbf{B}_w$ becomes negligible and the stimulated currents, although small, are mainly due to $\mathbf{E}_w$ acceleration.

For some electrons, the bunching force is strong enough to cause the electron's $\mathbf{v}_\perp$ to oscillate about $-\mathbf{B}_w$. The frequency of this oscillation is called the trapping frequency and is given by

$$\omega_t = \sqrt{\frac{eB_w}{m}kv_\perp} \tag{17}$$

and the maximum velocity deviation of a trapped electron from v_R is called the trapping velocity and is given by

$$v_t = \frac{2\omega_t}{k} \tag{18}$$

More detailed discussions of trapping can be found in *Dysthe* [1971], *Nunn* [1971], and *Matsumoto* [1979].

As long as the field seen by some of the electrons is approximately stationary, the interaction can yield significant phased bunched currents. The phase bunched current can be represented by a current sheet given by the vector sum of all perpendicular velocities within a slab of thickness Δz. The current per unit slab thickness is thus given by

$$\mathbf{J}_R(z,t) = -e\int_\phi\int_\alpha\int_v \mathbf{v}_\perp(z,t)f(v,\alpha)v^2\sin\alpha dv d\alpha d\phi \quad \left(\mathrm{A/m^2}\right) \tag{19}$$

Each current sheet launches a wave in both directions. All such current sheets act like an end-fire antenna array in that there is substantial addition of coherent radiation only in the direction of wave propagation (opposite to $v_\parallel$) [*Brice*, 1963; *Helliwell and Crystal*, 1973]. The field radiated from the current sheet in the direction of wave propagation is

$$\Delta\mathbf{B}_s(z,t) = \frac{\mu_0}{2}\left[\mathbf{J}_R(z+\Delta z/2,t)\times\mathbf{n}\right]\Delta z \tag{20}$$

where $\mathbf{n}$ is the unit vector in the $\mathbf{k}$ direction and the point z is taken just outside the current sheet centered at $z+\Delta z/2$. These vector relationships are shown in Figure 5. The total radiation at a given point in space is

$$\mathbf{B}_w(z,t) = \mathbf{B}_{in}(z,t) + \mathbf{B}_s(z,t) + \Delta\mathbf{B}_s(z,t) \tag{21}$$

which is the sum of the externally applied or input wave $\mathbf{B}_{in}$, the stimulated radiation associated with the local current sheet $\Delta\mathbf{B}_s$, and the radiation that has propagated to this point in space from other current sheets $\mathbf{B}_s$. Since Δz is not vanishingly small, (21) implies a discrete method of updating the total wave field. For a wave propagating in the $-z$ direction,

$$\mathbf{B}_w(z-\Delta z, t+\Delta t) = \mathbf{B}_w(z,t) + \Delta\mathbf{B}_s(z,t) \tag{22}$$

where $\Delta t = \Delta z/v_g$. In other words, the wave would be propagated, then updated by adding $\Delta\mathbf{B}_s$, then propagated, and so on. Equation (22) is the basis for the wave growth model detailed in the next section.

From equations (22) and (20) an expression can be derived for the growth rate defined as

$$\Gamma = \frac{1}{B_w}\frac{dB_w}{dt} \tag{23}$$

The resonant current $\mathbf{J}_R$ can be decomposed, as shown in Figure 5, into two components $\mathbf{J}_B$ and $\mathbf{J}_E$, which are parallel and perpendicular to $\mathbf{B}_w$, respectively. From (20), $\mathbf{J}_E$ will generate a $\Delta\mathbf{B}_s$ antiparallel to $\mathbf{B}_w$ while $\mathbf{J}_B$ will generate a $\Delta\mathbf{B}_s$ perpendicular to $\mathbf{B}_w$ in the direction of $\mathbf{E}_w$. Thus, for $\Delta B_s << B_w$, $\mathbf{J}_E$ changes the wave amplitude and $\mathbf{J}_B$ changes the wave frequency which makes

$$\Gamma = \frac{1}{B_w^2}\frac{\Delta\mathbf{B}_s\cdot\mathbf{B}_w}{\Delta t} = -\frac{\mu_0}{2}v_g\frac{J_E}{B_w} \tag{24}$$

This same expression can be derived more rigorously from Maxwells equations and the linearized momentum equation for the cold electrons [*Omura and Matsumoto*, 1982].

The electric field component $\mathbf{E}_w$, can be calculated from Maxwells equation. For a growing wave, it is clear from Maxwells equations that the angle between $\mathbf{B}_w$ and $\mathbf{E}_w$ deviates from 90°. The deviation angle $\delta\beta$, indicated in Figure 5, is given by

$$\delta\beta = \tan^{-1}\left(\Gamma/\omega\right) \tag{25}$$

From the "reference" simulation presented in a later section, an extreme value for $\delta\beta$ of 0.17° was calculated by substituting into (24), the peak magnitude of J_R for J_E, the applied wave intensity B_{in} for B_w, and the equatorial group velocity for v_g. The actual deviation angles for the simulations in this paper will be closer to 0° and thus, its effect in the calculation of $\mathbf{J}_R$ is negligible [*Omura and Matsumoto*, 1982].

Small deviation angles is also a necessary, though not sufficient, criterion for the applicability of cold plasma theory to wave propagation. From Maxwell's equations, the total current must be parallel to $\mathbf{B}_w$. The total current $\mathbf{J}$ is the vector sum of the resonant current $\mathbf{J}_R$ and the cold plasma current $\mathbf{J}_C$, given by

$$\mathbf{J}_C = \frac{k\mathbf{B}_w}{\mu_0} \tag{26}$$

Since $J_R << J_C$ in the simulations to follow, the effect of $\mathbf{J}_R$ on wave propagation can be neglected. Thus, for the purposes of propagating the wave, cold plasma theory applies (i.e. $\mathbf{J} = \mathbf{J}_C$ and $\mathbf{B}_w \perp \mathbf{E}_w$).

3. SIMULATION MODEL

The previous section detailed the basic equations relating to the wave growth process. However, in order to feasibly perform wave growth simulations, the simulation parameters must be constrained (the typical simulation in this paper consumed about 5 hours of VAX/780 CPU time). In paticular, the interaction region must be truncated, the wave update method simplified, and the electron distribution limited. These impositions are discussed briefly in this section, and in more detail by *Carlson* [1987].

Interaction Region

The space-time relationships of the model are summarized in Figure 7. Wave-particle interactions are computed in the region between the upstream and downstream boundaries z_{up} and z_{down}, respectively. The wave enters the region at the downstream boundary and exits at the upstream boundary. As the leading edge of the wave propagates across the region, electrons are injected into the leading edge at Δz km spacings. However, after the leading edge crosses the upstream boundary, electrons are injected at the upstream boundary at Δt second intervals (defined later). Short arrows in Figure 7 indicate these particle injection points. Letting z_i represent the position at which the ith set of electrons enters the wave, then

$$z_i = \begin{cases} z_{down} - i\Delta z & \text{for } z_{down} - i\Delta z > z_{up} \\ z_{up} & \text{otherwise} \end{cases} \quad (27)$$

Calculations performed in the next section were carried out using $z_{down} = 2150$ km, $z_{up} = -1350$ km, and $\Delta z = (z_{down} - z_{up})/285 \simeq 12.3$ km.

In order to avoid 'step responses' caused by injecting electrons at the boundary, an upstream boundary taper is applied to the wave field. A similar spatial taper is applied to the phase bunched currents near the downstream boundary in order to reduce the phase noise in the stimulated radiation near this boundary. This phase noise, without the downstream current taper, can excite numerical instabilities which propagate through the region, destroying the coherent wave growth. These tapers are depicted as weighting factors at the top of Figure 7.

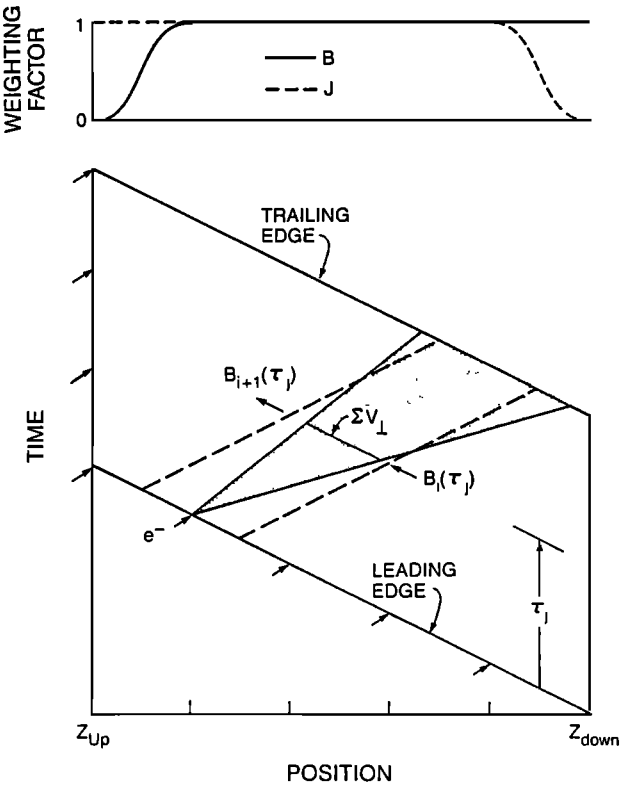

Fig. 7. Summary sketch of the space-time relationships of the transient model. The wave enters at the downstream boundary z_{down}, and exits at the upstream boundary z_{up}. Electrons are injected (arrows) into the wave at the leading edge and at the upstream boundary. An upstream boundary taper is applied to the wave field and a downstream taper is applied to the phase bunched currents as indicated by the weighting factors (top). The current is calculated by summing the $\mathbf{v}_\perp$'s at equally spaced τ's. The radiation from these currents propagates forward and is seen by the next set of injected electrons.

Wave Field Update

A few approximations involving the wave update process can greatly reduce the computer resources required to perform a simulation. As discussed in the last section, choosing the applied wave frequency to be one-half the equatorial electron gyrofrequency allows, to a good approximation, all of the radiation to be propagated at the group and phase velocity of the applied wave. Thus, stimulated radiation can simply be added to the applied wave and then propagated without incurring a phase shift. In other words, radiation added to the wave τ-seconds into the pulse remains at τ-seconds into the pulse as the wave propagates. As indicated in Figure 7, τ is defined at any position z to be the time since the arrival of the wave leading edge.

Regarding feedback, it can be assumed that radiation from electrons injected into the wave at earlier times only feeds back on subsequently injected electrons. Conversely, electrons will not see any radiation from electrons injected at the same time or at later times. This approximation is justified since $\Delta B_s << B_w$.

Calculating the current (19) and stimulated radiation (20) requires the integration over $\mathbf{v}_\perp$ within each spatial cell at each instant. However, electrons injected at the same point in space and time arrive at some downstream point in space with a range of times. This "fan out" is illustrated in Figure 7 and is due to the spread in $v_\parallel$ and α of the injected electrons and also due to cyclotron phase dependent wave forces (For electrons with $v_{\parallel eq} = v_{Req}$ and α_{eq} of 6° and 72°, the fan out is less than 4 ms at the equator if injected at z_{up}). One way to get the electron distribution at a point in space and time is to look at the trajectories of two sets of electrons with the same unperturbed distributions, but with two different injection points, and interpolate. This technique was actually employed but only to verify the accuracy of a simpler approach. This simpler approach determines the electron velocities at equally spaced τ's by interpolating along each particle's trajectory. The current is then calculated by summing the $\mathbf{v}_\perp$'s at each τ for all electrons entering the wave at the same injection point, even though these electrons are at different points in space and time. Electrons entering the wave at the same injection point are taken to represent all of the electrons which would have entered the wave since the previous injection. Incorporating this approximation into the combined form of equations (19) and (20), the stimulated radiation versus τ from the electrons entering the wave at the ith injection point becomes

$$\Delta \mathbf{B}_{si}(\tau) = -\frac{e\mu_0}{2} \int_\phi \int_\alpha \int_v \left[\mathbf{v}_{\perp i}(\tau) \times \mathbf{n}\right] v_{\parallel_i}(\tau) \Delta t_i \cdot f(v,\alpha) v^2 \sin\alpha \, dv \, d\alpha \, d\phi \quad (28)$$

where $v_{\parallel_i}(\tau)\Delta t_i$ and Δt_i are the spatial and temporal separations, respectively, of an electron from its previously in-

jected counterpart. When the electrons are injected into the leading edge

$$\Delta t_i = \Delta z \left(\frac{1}{v_{\|}(z_i)} + \frac{1}{v_g(z_i)} \right) \tag{29}$$

however, when the electrons are injected at the upstream boundary

$$\Delta t_i = \frac{2\Delta z}{v_g(z_{\mathrm{up}})} \tag{30}$$

since the leading edge is advanced an equivalent of two Δz steps per injection in order to keep Δt_i about the same in both cases.

When the trajectories are calculated for all of the electrons injected at the ith injection point, $\Delta \mathbf{B}_{si}(\tau)$ is computed and added to the applied wave, giving the applied wave to be used at the $(i+1)$th injection point

$$\mathbf{B}_{wi+1}(\tau) = \mathbf{B}_{wi}(\tau) + \Delta \mathbf{B}_{si}(\tau) \tag{31}$$

Therefore, the wave update equation (22) has been recast into a form which is easier to compute.

Energetic Electron Distribution

In terms of the comparisons of our model results with experimental data, probably the most important determinant is the energetic electron distribution function. Computer processing time limitations allow only narrow $v_{\|}$ ranges to be considered. However, during the course of the interaction, the central $v_{\|}$ is varied in a way which maximizes the wave growth rate. The fact that the simulations reproduce some of the observed features suggests that the particles selected in this way are the ones that contribute most to the growth process. That a narrow range of electrons dominantly contribute to the wave growth is consistent with experimental data, which indicates that coherent signals with frequencies separated by ~ 100 Hz or more appear to grow independently [*Helliwell*, 1983].

The generalized form of the distribution function used is

$$f(v,\alpha) = Av^{-8} g(\alpha) h(v,\alpha) \tag{32}$$

or equivalently, in terms of $v_{\|}$ and $v_{\perp}$

$$f(v_{\|}, v_{\perp}) = A({v_{\|}}^2 + {v_{\perp}}^2)^{-4} g(v_{\|}, v_{\perp}) h(v_{\|}) \tag{33}$$

where $g(\alpha)$ (equivalent to $g(v_{\|}, v_{\perp})$) is a pitch angle anisotropy factor and $h(v_{\|})$ (equivalent to $h(v,\alpha)$) is the $v_{\|}$ sampling function. For the results in the next section, $g(\alpha) = 1$ and $h(v_{\|}) = \delta\left(v_{\|} - V_{\|}(z_i)\right)$ where $V_{\|}(z_i)$ is determined by a selection function. A distribution function of this form is generally able to excite whistler mode waves [*Bell and Buneman*, 1964].

As mentioned in the introduction, the purpose of the selection function is to vary the center velocity of the electron distribution so that the wave and electrons stay in resonance. The $V_{\|}$ determined by the selection function should ideally supply the "primary" wave-particle interactions. In our model of the wave growth process, the primary wave-particle interaction is first-order resonant as the wave propagates toward the equator, but switches to second-order resonant as the wave approaches and crosses the equator and a fixed interaction region is established. Therefore, the selection function needs to involve two cases. The first case selects electrons which, if unperturbed, satisfy the first-order resonance condition after moving a fixed distance z_{shift}, from the injection location. The second case selects electrons which, if unperturbed, would satisfy the second-order resonance condition at a fixed location z_{fix}, with a wave whose frequency is changing at a constant rate. In the simulations to follow a z_{shift} of 200 km was chosen as representative of the first-order resonant interaction region location, relative to the point at which the electrons entered the wave. From second order resonance theory z_{fix} is related to df/dt. An approximate expression for this relationship is

$$\frac{1}{z_{fix}} \frac{df}{dt} \simeq 1 \quad \left(\frac{\mathrm{Hz/s}}{\mathrm{km}} \right) \tag{34}$$

Choosing a value of z_{fix} which maximizes the wave growth rate is the basis of a maximum likelyhood technique described in the next section. The first case of the selection is used until $z_i + z_{shift} = z_{fix}$, after which the second form of the selection function is used. More specifically, the parallel velocity at the ith injection point is

$$V_{\|}(z_i) = \begin{cases} C_1 v_R(z_i + z_{shift}) & \text{for } z_i + z_{shift} \geq z_{fix} \\ C_2 \left(v_R(z_{fix}) - (i - i_{fix}) \Delta v_{\|} \right) & \text{otherwise} \end{cases} \tag{35}$$

where i_{fix} is the injection point index at which $z_i + z_{shift} = z_{fix}$, C_1 and C_2 are cosine ratios given by

$$C_1 = \frac{\cos(\alpha(z_i))}{\cos(\alpha(z_i + z_{shift}))} \tag{36}$$

$$C_2 = \frac{\cos(\alpha(z_i))}{\cos(\alpha(z_{fix}))} \tag{37}$$

which adiabatically translate the resonant velocities to injection parallel velocities, and $\Delta v_{\|}$ is the shift in parallel velocity required for the injected electrons to stay in resonance with a wave whose frequency changes at the rate df/dt. $\Delta v_{\|}$ is approximated by

$$\Delta v_{\|} \simeq \Delta t_i \frac{dv_{R\mathrm{eq}}}{dt} \tag{38}$$

$$\simeq \Delta z \left(\frac{1}{v_{g_{\mathrm{eq}}}} + \frac{1}{v_{R\mathrm{eq}}} \right) \frac{2\pi}{k_{\mathrm{eq}}} \left(1 + \frac{f_{H\mathrm{eq}}}{2f} \right) \frac{df}{dt} \tag{39}$$

In this formulation $\Delta v_{\|}$ is constant. However, in an exact solution, $\Delta v_{\|}$ would be slowly changing. When using a broad $v_{\|}$ sampling function rather than a delta function, the same selection function would be used and would apply to the center of $h(v_{\|})$.

4. RESULTS

In this section the model is tested using input parameters consistent with experimental observations. The energetic electron flux is set to give a total growth of ~ 38 dB and a growth rate of ~ 150 dB/s. These values of growth and growth rate are slightly larger than what is usually observed. However, since saturation occurs within a shorter period of time, shorter wave pulses can be used resulting in reduced

CPU time. Also, the growth tends to be more exponential and the amplitude fluctuations reduced, as the growth rate is increased. The actual input parameters used are given in Table 1.

TABLE 1. Simulation Parameters

Parameter	Value	
f	1/2	f_{Heq}
B_{ineq}	0.01	pT
n	8	
α	6°-72° by 3°	
Φ_{E_0}	1.7×10^9	$(m^2 s\ ster\ keV)^{-1}$
E_0	1	keV
z_{up}	−1350	km
z_{down}	2150	km
Δz	~ 12.3	km
z_{fix}	30	km
z_{shift}	200	km
Downstream current taper	200	km
Upstream field taper	300	km
Pulse duration	500	ms
Front end taper	50	ms
Injection points	506	
Electrons/Injection	276	
Electrons	139656	

As a check, the model was tested by reproducing some of the results published by *Helliwell and Crystal* [1973] for a homogeneous static magnetic field. However, all of the results presented here include the inhomogeneity of the dipole magnetic field. Also, it is interesting to note that the results of *Helliwell and Crystal* [1973] were obtained using a 16-port model. Their concept of a port, although not exactly equivalent, is analogous to the number of spatial steps used in the present model which, for most of the results presented here, employed 200-300 steps. This larger number of spatial steps is required to adequately sample the spatial rotations in the current caused by the inhomogeneity. Using the parameters given in Table 1, simulations are performed. Magnitude and phase surfaces of the total wave field, including wave growth, are shown in Figure 8 and the associated magnitude and phase surfaces of the phase-bunched current are shown in Figure 9. The phase in Figure 8 is the phase of $\mathbf{B}_w$ relative to $\mathbf{B}_{in}$ while the phase in Figure 9 is the phase of $\mathbf{J}_R$ relative to $\mathbf{B}_w$. The magnitude surface in Figure 8 shows the leading and trailing edges propagating through space with increasing time. The leading edge is slightly shaped in order to approximate an actual pulse and to reduce the step response of injected electrons. In contrast, the trailing edge is abrupt since it represents the point at which electron trajectory calculations are terminated rather than the trailing edge of the actual pulse. These surfaces show that the current, and hence stimulated radiation, is generally confined to the equatorial region, between −500 km and 500 km. Examination of $\mathbf{B}_w(t)$ at the upstream boundary shows that the output wave field grows exponentially up to a saturated level while the phase advances quadratically with time and thus, the frequency increases linearly with time. Furthermore, the phase surface clearly shows an upstream temporal phase advance evolving from the downstream spatial phase advance due to the geomagnetic inhomogeneity.

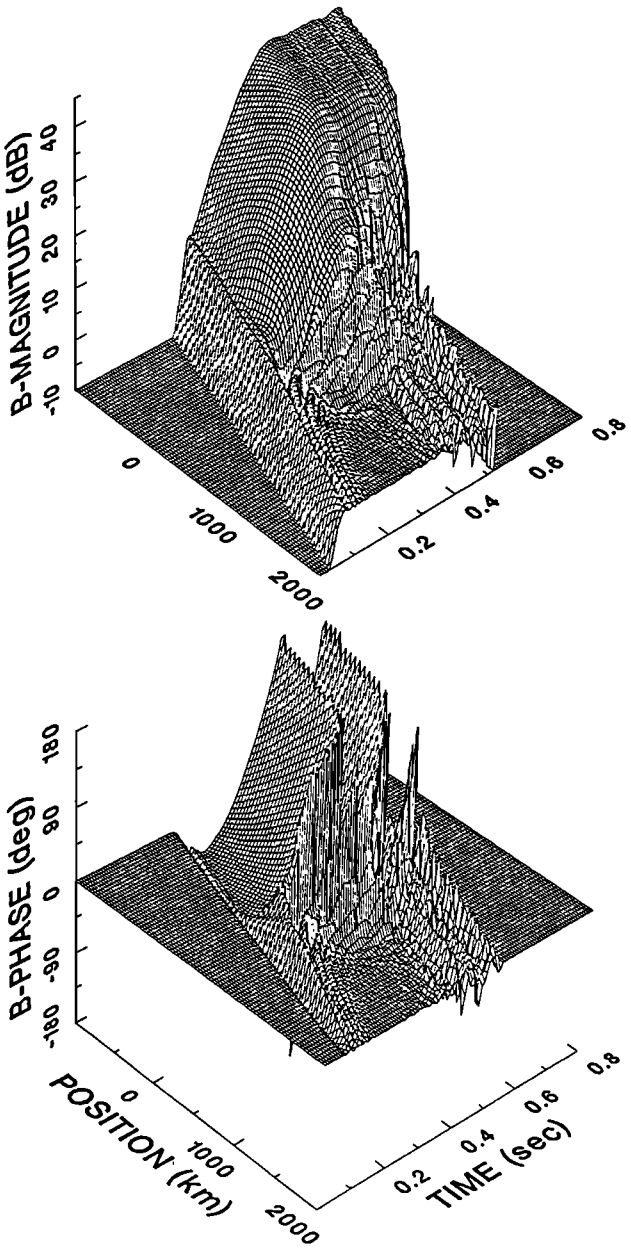

Fig. 8. Magnitude and phase surfaces of $\mathbf{B}_w$ from the wave growth simulation using the parameters in Table 1. The phase surface is the phase of $\mathbf{B}_w$ relative to $\mathbf{B}_{in}$. Exponential growth, saturation, and parabolic phase advance are seen at the upstream boundary while the applied wave is seen at the downstream boundary. Wave growth is confined to the equatorial region. The temporally advancing output phase results from the spatially advancing wave phase, induced by the geomagnetic inhomogeneity in the downstream region, feeding back on the resonant electrons.

The lack of wave growth in the downstream region results from the effects of phase mixing in this inhomogeneous region. The enhanced level of noise-like stimulated radiation at high τ's in this downstream region is associated with the currents near the downstream boundary and does not appear to be growing in the region away from this boundary. The possibility of a buildup of noise in the downstream region being related to some of the observable physical phenomena (e.g. saturation, triggering, sidebands) should be recognized.

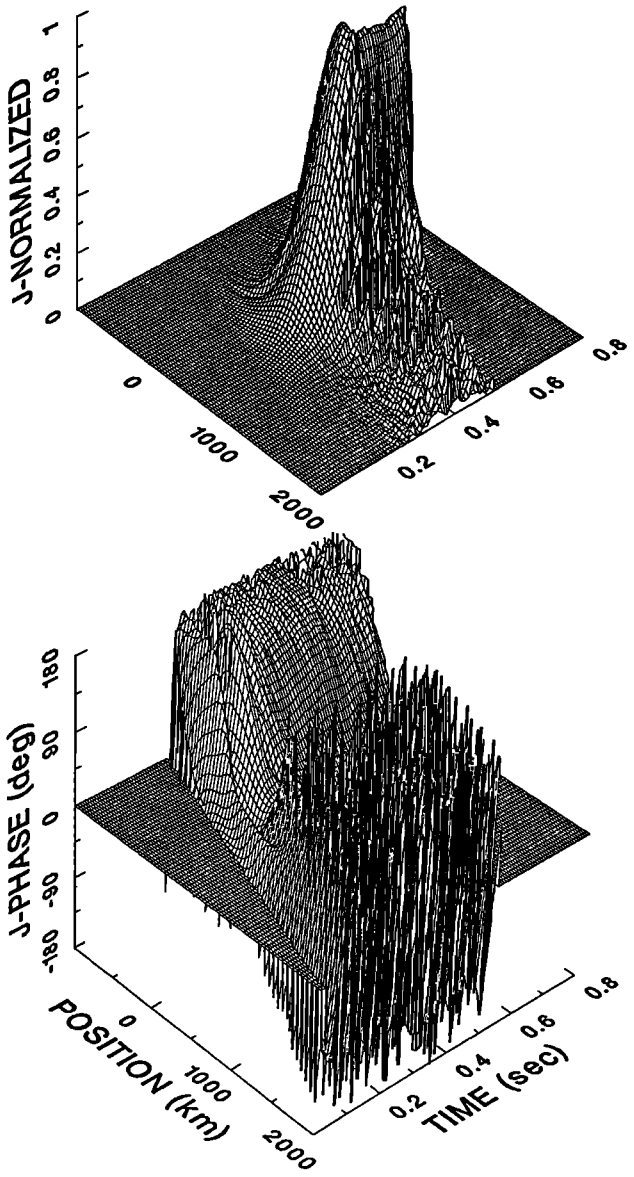

Fig. 9. Magnitude and phase surfaces of the current $\mathbf{J}_R$, which is responsible for the wave growth seen in Figure 8. The phase surface is the phase of $\mathbf{J}_R$ relative to $\mathbf{B}_w$. The confinement of the current to the equatorial region results from the phase mixing effects of the inhomogeneity.

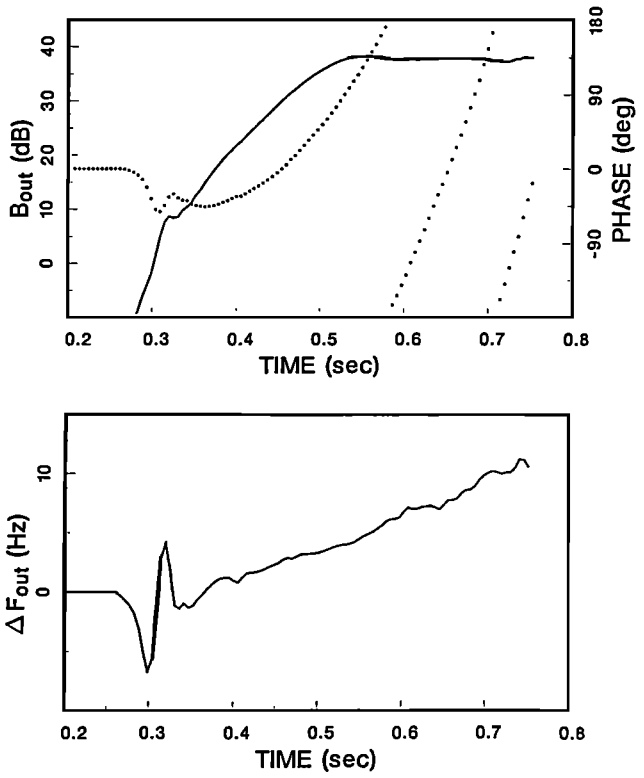

Fig. 10. Output wave magnitude and phase (top panel, solid and dotted respectively) versus time corresponding to $\mathbf{B}_w$ at the upstream boundary of Figure 8. The magnitude plot (referenced to $B_{in} = 0.01$ pT) shows $\sim$ 8 dB of spatial growth resulting from the 'step response' current, followed by $\sim$ 150 dB/s exponential growth up to a saturated level of $\sim$ 38 db. The phase is advancing at a nearly parabolic rate. Also shown is the instantaneous frequency (bottom panel) calculated by taking the derivative with respect to time of the wave phase in the upper panel. This curve has been smoothed slightly by convolving with the 3 point sequence {0.25, 0.5, 0.25}. The frequency versus time shows a nearly linear increase in frequency at $\sim$ 30 Hz/s.

A ridge of wave growth along the leading edge of the wave shows the effect of introducing the electrons into the wave. This ridge grows by $\sim$ 8 dB and is due to the fact that, as electrons are introduced into the wave, they all experience the same 'kick' regardless of the leading edge position. Hence, $\mathbf{J}_R$ starts out aligned with $\mathbf{B}_w$ and then rotates, depending upon $v_\parallel$ and the inhomogeneity. Therefore, at small τ's (*i.e.* before this 'step response' phase mixes away), radiation grows coherently as the wave propagates. Further discussion regarding this 'step response' is given later in association with the phase retardation of the wave field near the leading edge.

Comparison of the wave growth predicted by this model with experimental observations can be made by looking at the output field at the upstream boundary $\mathbf{B}_w(z = z_{\rm up}, t)$. Figure 10 gives plots of the output wave magnitude and phase (top panel), and frequency shift (bottom panel) versus time. The magnitude plot clearly shows the $\sim$ 8 dB of spatial growth resulting from the 'step response' current, followed by $\sim$ 150 dB/s exponential growth up to a saturated level of $\sim$ 38 dB. The exponential growth results from the self sustaining feedback process. The saturation appears to result from fully bunching most of the electrons within the equatorial interaction region. While this effect provides a plausible mechanism for saturation were the available particles limited to those considered in the simulation, it is not known whether the experimentally observed saturation would be due mainly to the same phenomenon. As the wave intensity increases, it would be expected that particles in an increasingly wider $v_\parallel$ range would be significantly perturbed which might provide continuing energy to the wave. Simulation results are given later from a first attempt at including a range of parallel velocities. While this simulation yielded a comparable saturation level ($\sim$ 36 dB), a limited $v_\parallel$ range was utilized and the $v_\parallel$ spacing was fairly coarse (approximately equal to the trapping velocity). Therefore, the mechanism for saturation remains to be confirmed.

The wave phase in Figure 10 is oscillatory, but generally retarding prior to the onset of parabolically advancing phase. This retarding phase results directly from the step

response current being initially aligned with $\mathbf{B}_w$, generating a lagging $\mathbf{B}_s$ which retards the wave phase and is reinforced by feedback to subsequent electrons. However, if a wider range of $v_\parallel$'s were included, this would promote more rapid phase mixing of the step response current which is expected to reduce the time over which the wave phase is retarding. In the limit as the $v_\parallel$ range is increased to a full distribution, the phase could start advancing instantaneously from some new offset reference. In other words, the initial phase retardation could actually be the hot plasma contribution to the refractive index. This would explain why phase retardation like that shown in Figure 10 is not commonly seen in the actual measurements. Also, if an actual phase retardation existed over a time less than that shown in Figure 10, then it would be difficult to detect using presently available methods (E. W. Paschal, private communication, 1987).

Taking the derivative with respect to time of the wave phase gives the instantaneous frequency shown in Figure 10. This curve has been smoothed slightly by convolving with the 3 point sequence {0.25, 0.5, 0.25}. Examining the frequency versus time plot after the advancing phase is established, shows a nearly linear increase in frequency at $\sim$ 30 Hz/s, consistent with the chosen $v_\parallel$ selection function and second order resonance theory.

Maximum Likelihood Test

The 30 Hz/s frequency drift rate not only compares to measured drift rates, but also satisfies a maximum likelihood test. The maximum likelihood test is an answer to the following question: At what frequency drift rate do the energetic electrons give up their energy at a maximum rate? The results from several simulations performed using different z_{fix}'s are superimposed in Figure 11 and clearly show a df/dt dependent growth. To better see which df/dt gives the fastest growth, amplitude versus df/dt, parametric in τ, is plotted in Figure 12. This figure shows a well defined peak in the amplitude versus df/dt curves at a df/dt of $\sim$ 30 Hz/s.

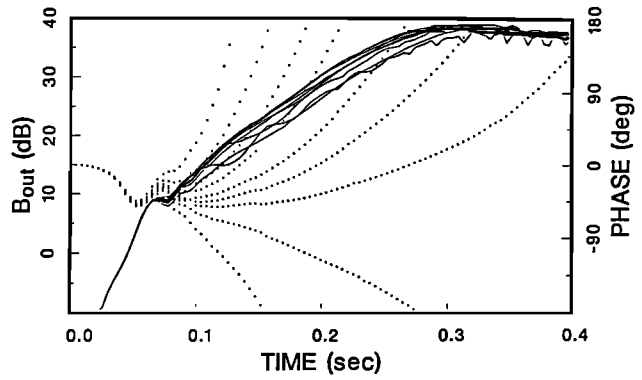

Fig. 11. Output magnitude (solid) and phase (dotted) from several simulations, with different injection $v_\parallel$ selection functions designed to support df/dt's of -40, 0, 20, 30, 40, 60, 80, 120, and 200 Hz/sec. These curves indicate that one selection function yields a higher average growth rate than the others. This is the basis for a maximum likelihood test which suggests that the selection function resulting in the fastest growth, represents the dominant mode of growth. The results are better displayed in Figure 12 in which amplitude versus df/dt are plotted parametric in time.

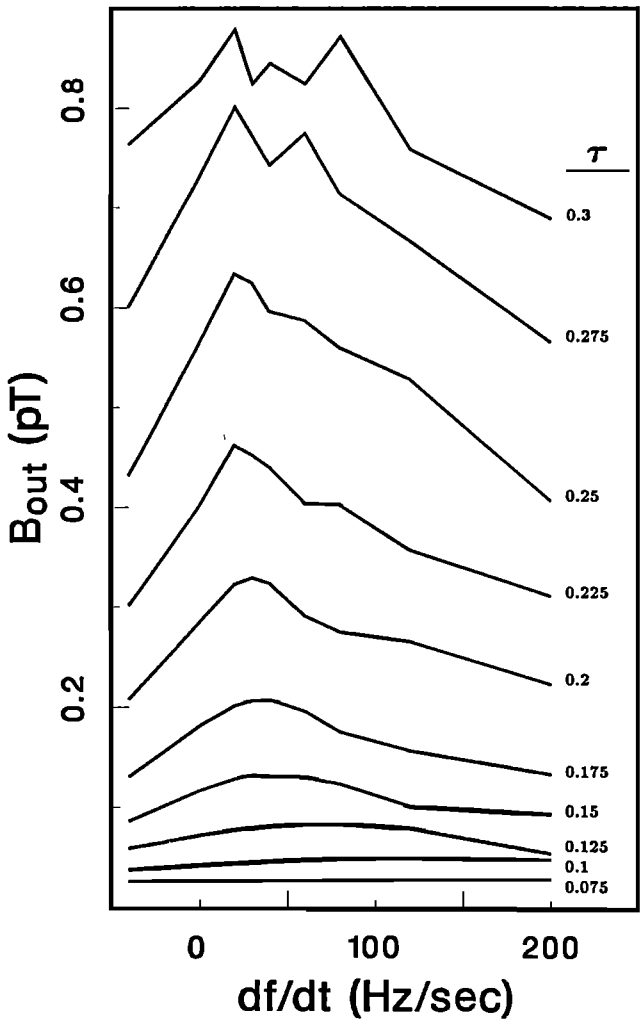

Fig. 12. Output amplitude of the simulations of Figure 11 versus df/dt parametric in τ (the time from the leading edge). df/dt is the rate of frequency increase in the injection velocity selection function. The peak in the curves at a df/dt of $\sim$ 30 Hz/s indicates the fastest growing case and should therefore be the dominant mode of growth. This outlines the maximum likelihood test for determining the injection $v_\parallel$ selection function and the mode of growth.

Thus, Figure 12 indicates that $\sim$ 30 Hz/s is the maximum likelihood rate of frequency increase and should be the dominant mode of growth. So not only does this model reproduce the proper frequency advance but, for the same parameters, it maximizes the rate at which energy is extracted from the energetic electrons.

Self Excited Emissions

The maximum likelihood test described above can be applied to experimentally observed self excited emissions triggered by short pulses. Termination of an applied signal can result in a triggered rising or falling emission but most likely a faller, especially if the pulse terminates before saturation. Rising emissions can also be triggered prior to termination but generally after saturation or coincident with the end of growth. Falling emissions can be triggered not only by the

termination of monochromatic waves but also by the beating of two monochromatic waves at closely spaced frequencies [*Helliwell et al.*, 1986*a*]. The falling emission, or 'faller', is established after a rapid increase in frequency associated with a band limited impulse coincident with pulse termination. However, application of the maximum likelihood test, using a 100 msec applied pulse, showed no evidence of a dominant emission form. By second order resonance theory, a falling emission is generated by an interaction region that drifts upstream of the equator. The possibility of this drift is not included in the injection velocity selection function as given in equation (35). From second order resonance theory, an interaction region drifting at a nearly constant rate will result in a wave frequency changing at nearly a parabolic rate.

Parameter Dependencies

In the following simulations we investigate the dependence of wave growth upon other parameters. While the assumed df/dt should be based upon the maximum likelihood test outlined above, for all of the following simulations a 30 Hz/s df/dt is assumed. The parameters to be varied include the applied wave intensity, energetic electron flux, pitch angle distribution, and parallel velocity range. Amplitude and phase versus time are plotted parametric in the varied parameter. All of these plots include the 30 Hz/s case shown in Figure 11 for comparison and hereafter refered to as the "reference" case. A summary of the dependence of growth rate and saturation level upon the varied parameter is given in Table 2. The growth rate and saturation level values are estimates made from the amplitude versus time plots. This table also includes the results from the self excited emission case (100 ms pulse) and the 30 Hz/s, or "reference", case (Table 1 parameters).

TABLE 2. Growth Rate and Saturation Levels

Case	Growth Rate (dB/s)	Saturation Level (dB)
Table 1 parameters	156	38
100 msec pulse	143	38
B_{in} = 0.001 pT	151	38
B_{in} = 0.1 pT	163	38
Flux Doubled	268	43
Flux Halved	58	24
$g(\alpha)\Big\|_{a=x=0.2,y=12}$	186	39
$g(\alpha)\Big\|_{a=x=0.2,y=2}$	214	40
Broad $h(v_\parallel)$	79	36

Dependence on Applied Wave Intensity

Amplitude and phase versus time, parametric in applied wave intensity B_{in}, are given in Figure 13. Again, these represent the wave magnetic field at the output, or upstream side of the interaction region. In addition to the reference case (Table 1 parameters) with a B_{in} of 0.01 pT, applied wave intensities of 0.001 and 0.1 pT are included in Figure 13. In accord with the results of *Helliwell and Crystal* [1973] for a homogeneous medium, Figure 13 indicates that growth rate and saturation level are not significantly dependent upon applied wave intensity. These results imply that growth would result even from an infinitesimally small input wave suggesting that the amplitude threshold for wave growth phenomena might be associated with the interfering noise that is always present in the magnetosphere. The phase curves in Figure 13 show that the phase tends to advance more slowly for higher B_{in}'s. This same trend is associated with increasing growth rate in the figures to follow.

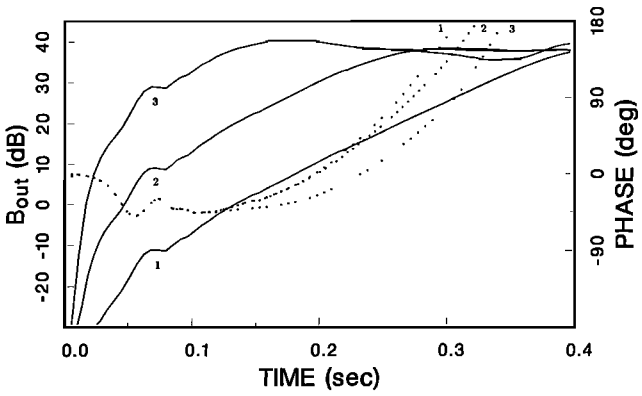

Fig. 13. Output amplitude (solid) and phase (dotted) versus time, parametric in applied wave intensity (referenced to B_{in} = 0.01 pT). The applied wave intensities of 0.001, 0.01 (reference case, same as Figure 10), and 0.1 pT are labeled 1, 2, and 3 respectively. These curves indicate that growth rate and saturation level are not significantly dependent upon applied wave intensity. The phase curves show that the phase tends to advance more slowly for higher B_{in}'s. This same trend is associated with increasing growth rate in later figures.

Dependence on Energetic Electron Flux

Figure 14 shows the effect varying the energetic electron flux has on growth. In addition to the reference case, two

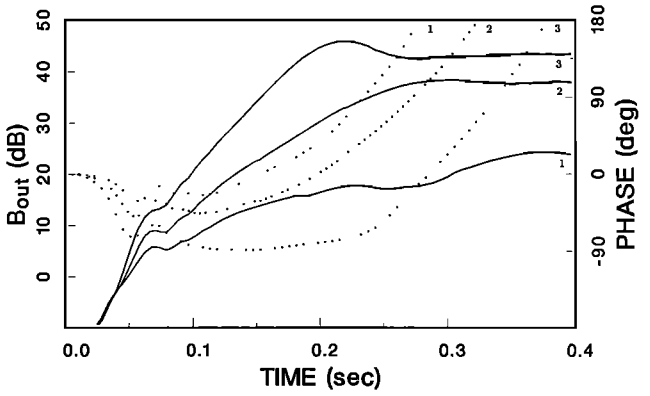

Fig. 14. Output magnitude (solid) and phase (dotted) parametric in energetic electron flux. In addition to the reference case (2, same as Figure 10), two other cases are shown having half (1) and twice (3) the energetic electron flux as the reference case. The growth rate and saturation level both increase with increasing flux while the phase tends to advance more slowly with increasing growth rate.

other cases are shown having half and twice the energetic electron flux as the reference case. In the self excited homogeneous case (*Helliwell and Crystal*, 1973), the saturation level increases with increasing flux but the change in saturation level with respect to flux decreases with increasing flux. From Table 2, the same relationship between saturation level and flux is displayed. However, the change in growth rate with respect to flux is also found to be decreasing with increasing flux. This difference could be due either to the presence of the applied wave or to the inhomogeneity. Also, as mentioned before, the phase tends to advance more slowly with increasing growth rate.

The Role of the Pitch Angle Anisotropy

In all of the simulation results shown so far, a unity pitch angle anisotropy factor ($g(\alpha) = 1$) has been used. Figure 15 compares the reference case with two distribution functions having more anisotropic pitch angle factors, $g_1(\alpha)$ and $g_2(\alpha)$. These $g(\alpha)$'s have the form

$$g(\alpha) = a \sin^x \alpha + (1-a)\sin^y \alpha \tag{40}$$

Both have $a = x = 0.2$ but $y = 2$ in $g_1(\alpha)$ and $y = 12$ in $g_2(\alpha)$. The effect of these functions is to concentrate more of the electrons at higher pitch angles. Because changing $g(\alpha)$ alters the number density, the distribution function must be rescaled for each $g(\alpha)$ so that the number densities are the same. Since the form of the distribution function used (32) is separable, the number density equation can be rewritten

$$N(z) = 2\pi \int_{\alpha} g(\alpha)\cos^{n-3}\alpha \sin\alpha d\alpha \int_{v_\parallel} h(v_\parallel) v_\parallel^{-n+2} dv_\parallel \tag{41}$$

A general expression for $g(\alpha)$ which can be integrated in the above equation is

$$g(\alpha) = \sum_i \left(a_i \sin^{x_i}\alpha + b_i \cos^{y_i}\alpha\right) \tag{42}$$

performing the pitch angle integration

$$\int_{\alpha_{lc}}^{\pi/2} g(\alpha)\cos^{n-3}\alpha\sin\alpha d\alpha \simeq$$

$$\sum_i \left(a_i \left[\frac{\Gamma\left(\frac{n}{2}-1\right)\Gamma\left(\frac{x_i}{2}+1\right)}{2\Gamma\left(\frac{n+x_i}{2}\right)} - \frac{\alpha_{lc}^{x_i+2}}{x_i+2} \right] + b_i \left[\frac{2}{y_i+n-2} - \frac{\alpha_{lc}^2}{2} \right] \right) \tag{43}$$

where α_{lc} is the loss cone pitch angle and is assumed to be small enough to justify the small angle approximation to the value of the integrand at this angle, and where the following conditions must also hold:

$$n > 2, \quad x_i > -2, \quad y_i > 2 - n \tag{44}$$

Thus, the distribution function must be scaled by factors of 2.7 and 5.6 for $g_1(\alpha)$ and $g_2(\alpha)$, respectively. Examination of Figure 15 shows that this rescaling results in approximately the same saturation levels. The most interesting new feature is the fact that $g_1(\alpha)$ resulted in the largest growth rate. This can be explained in terms of $dg(\alpha)/d\alpha$ and the falloff of the number of electrons with increasing energy through the v^{-8} term. Large values of $dg(\alpha)/d\alpha$ are known, by linear theories, to drive the whistler mode instability. But, through the balancing of the $\mathbf{v} \times \mathbf{B}$ forces with the v^{-n} falloff in the electron distribution, $\sim 45^\circ$ pitch angle electrons are the largest fractional contributors to the total radiation. Therefore, since $dg_1(\alpha)/d\alpha$ has a maximum at $\sim 45^\circ$, it is not surprising that $g_1(\alpha)$ results in the largest growth rate. Although $dg_2(\alpha)/d\alpha$ actually has a greater maxima, it occurs at higher α's where the contribution to growth is less significant. Again, the phase tends to advance more slowly with increasing growth rate.

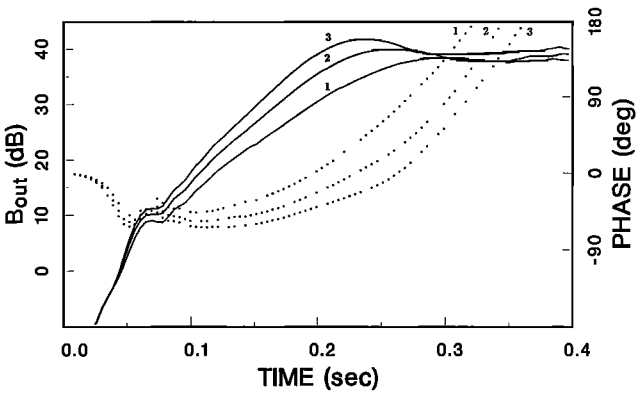

Fig. 15. Output magnitude (solid) and phase (dotted) parametric in pitch angle anisotropy $g(\alpha)$. The $g(\alpha)$'s are 1 (reference case, same as Figure 10), $0.2\sin^{0.2}\alpha + 0.8\sin^{12}\alpha$, and $0.2\sin^{0.2}\alpha + 0.8\sin^2\alpha$ and are labeled 1, 2, and 3 respectively. The distribution function has been rescaled for each $g(\alpha)$ so that the number densities are the same, resulting in nearly equal saturation levels. $g(\alpha) = 0.2\sin^{0.2}\alpha + 0.8\sin^2\alpha$ resulted in the largest growth rate presumably due to a maximum in $dg(\alpha)/d\alpha$ occuring at $\alpha \simeq 45^\circ$, the pitch angle of maximum radiation.

Effect of Increasing the Parallel Velocity Range

Some preliminary results were obtained using a range of $v_\parallel$'s. Specifically,

$$h(v_\parallel) = \sum_{j=-4}^{4} \left(a_j \delta(v_\parallel - v_\parallel(z_i) - j\Delta v_\parallel) \right) \tag{45}$$

where $\Delta v_\parallel = v_{Req}/800$ and $a_j = 1 - 0.2|j|$. This results in a triangular $v_\parallel$ distribution with a full width of 1.25% v_{Req} and a center $v_\parallel$ given by the selection function (35). This case is shown, along with the reference case, in Figure 16. Without rescaling to compensate for the 9 times greater number density, the resultant saturation level is comparable to the reference case. This is a direct result of the cancellation associated with the integration over $v_\parallel$. The $v_\parallel$ integration also reduced the growth rate by nearly a factor of 2. Overall, the key features continued to be reproduced, providing further evidence that the actual growth and saturation mechanisms are being simulated. However, more simulations, having broader $v_\parallel$ ranges and closer $v_\parallel$ spacings, are required before any final conclusions can be made. In this case, the $v_\parallel$ spacing is approximately equal to the

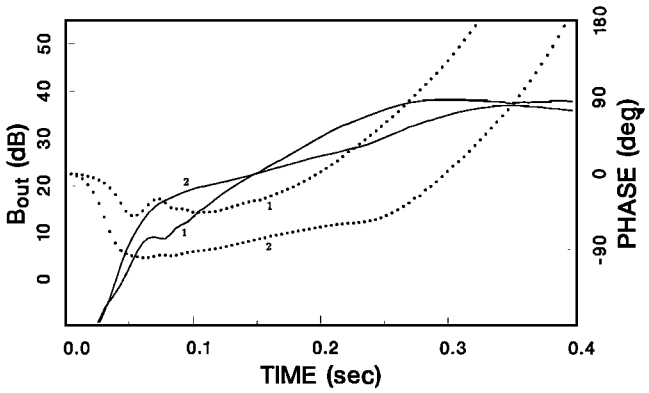

Fig. 16. Output magnitude (solid) and phase (dotted) parametric in parallel velocity windowing function $h(v_{\|})$. In addition to the reference case (1, same as Figure 10), another case is shown (2) which resulted from a triangular $v_{\|}$ distribution having a full width of 1.25% v_{Req}. Without rescaling to compensate for the 9 times greater number density, the resultant saturation level for the broad $v_{\|}$ case (2) is comparable to the reference case (1). This is a direct result of the cancellation associated with the integration over $v_{\|}$. The $v_{\|}$ integration also reduced the growth rate by nearly a factor of 2.

trapping velocity at the center of the interaction region for the saturated wave. To determine the distribution necessary to perform an adequate simulation, successive simulations should be performed with broader ranges and finer spacings until a repeatable solution is converged upon. One feature of the $v_{\|}$ integration which seems to improve the fit with the experimental measurements, is the onset of a stable phase advance at an earlier time.

5. Summary and Discussion

A new model is developed, based upon test particle trajectory calculations, to simulate the whistler-mode wave growth process. The simulations reproduce exponential wave growth and saturation coincident with a linearly increasing frequency versus time using applied wave intensities consistent with satellite measurements.

With this model the space-time evolution of a wave pulse can be simulated, with high spatial and temporal resolution, as the pulse propagates across the inhomogeneous equatorial region. Generalized equations of motion allow for the evolution of the frequency and wave number in space and time. Since only a narrow range of parallel velocities can be included, a scheme is developed to make the center $v_{\|}$ vary with the time and location at which the electrons are introduced into the wave. This relationship is called the selection function. For a class of selection functions consistent with second order resonance theory, a maximum likelihood test is developed which determines the function that maximizes the average growth rate. This test shows that, when an applied signal is present, the total wave phase at the output of the interaction region advances with time. The frequency increase is found to result from the feedback of radiation from the phased bunched currents which are rotated by the geomagnetic inhomogeneity. In other words, the maximum-likelihood selection function suggests that the most significant electrons are those which satisfy the second-order resonance condition for the observed frequency increase. The simulations also show how characteristic features such as growth rate and total growth, depend upon the various parameters such as applied wave intensity, energetic electron flux, pitch angle anisotropy, and the width of the $v_{\|}$ range.

Comparison of the simulations with actual experimental measurements show good agreement in growth rates, total growth, the rate of frequency increase, and even the period of amplitude and frequency oscillations. A simulation performed using a broader $v_{\|}$ range continued to reproduce growth and saturation, providing further evidence that the actual growth and saturation mechanisms are being simulated. In order to provide a better confirmation that the actual mechanisms are being simulated, future simulations should include broader, more densely sampled $v_{\|}$ ranges. A broader $v_{\|}$ range also seems necessary before triggered emissions can be produced.

The hypothesis regarding saturation is that the exhibited saturation results from the same mechanism demonstrated by *Helliwell and Inan* [1982]. This mechanism is related to the onset of trapping in that the electrons can become fully bunched within the interaction region when the time it takes the electrons to traverse the interaction region is greater than one-quarter of the trapping period. Further increases in the wave intensity can reduce the bunching time but cannot significantly increase the contribution to the output field by these electrons.

The simulations showed no indication of an amplitude threshold for growth as the applied wave intensity was varied. This suggests that the threshold phenomena might be associated with the interfering noise that is always present in the magnetosphere.

While self excited emissions generated at the termination of pulses are generally falling in frequency with time, this model and the implemented class of selection functions, showed no dominant emission form. However, in the self excited case, it is suggested that the selection function be modified to allow for an interaction region which can drift in space with time. By second order resonance theory, an interaction region drifting at a constant rate, can produce an emission whose frequency changes quadratically with time.

Acknowledgments. We would like to thank T. F. Bell and O. Buneman for their many valuable suggestions. This research was supported by the National Aeronautics and Space Administration under contract NGL-05-020-008 and by the Division of Polar Programs of the National Science Foundation under contracts DPP-83-17092 and DPP-83-18508.

The editor thanks three referees for their assistance in evaluating this paper.

References

Angerami, J. J., and J. O. Thomas, Studies of planetary atmospheres, 1, The distribution of electrons and ions inthe earth's exosphere, *J. Geophys. Res., 69*, 4537, 1964.

Artsimovich, L. A., and S. Y. Lukyanov, *Motion of charged particles in electric and magnetic fields*, MIR Publishers, Moscow, USSR, 1980.

Bell, T. F., The nonlinear gyroresonance interaction between energetic electrons and coherent VLF waves propagating in an arbitrary angle with respect to the earth's magnetic field, *J. Geophys. Res., 89*, 905, 1984.

Bell, T. F., The wave magnetic field amplitude threshold for nonlinear trapping of energetic gyroresonant and Landau resonant electrons by nonducted VLF waves in the magnetosphere, *J. Geophys. Res., 91*, 4365, 1986.

Bell, T. F., and O. Buneman, Plasma instability in the whistler mode caused by a gyrating electron stream, *Phys. Rev., 133*, A1300, 1964.

Bell, T. F., and U. S. Inan, Transient nonlinear pitch angle scattering of energetic electrons by coherent VLF wave packets in the magnetosphere, *J. Geophys. Res., 86*, 9047, 1981.

Brice, N. M., An explanation of triggered very-low-frequency emissions, *J. Geophys. Res., 68*, 4626, 1963.

Budden, J. G., *Radio Waves in the Ionosphere*, Cambridge University Press, New York, 1985.

Carlson, C. R., Simulation and modeling of whistler mode wave growth through cyclotron resonance with energetic electrons in the magnetosphere, Ph.D. thesis, Stanford University, Stanford, California, 1987.

Carlson, C. R., R. A. Helliwell, and D. L. Carpenter, Variable frequency VLF signals in the magnetosphere: associated phenomena and plasma diagnostics, *J. Geophys. Res., 90*, 1507, 1985.

Chang, H. C., Cyclotron resonant scattering of energetic electrons by electromagnetic waves in the magnetosphere, *Tech. Rep. E414-1*, p. 91, STARLAB, Stanford Electron. Lab., Stanford Univ., Stanford, Calif., 1983.

Chang, H. C., and U. S. Inan, Quasi-relativistic electron precipitation due to interactions with coherent VLF waves in the magnetosphere, *J. Geophys. Res., 88*, 318, 1983.

Das, A. D., and V. H. Kulkarni, Frequency-time structure of VLF emissions, *Planet. Space Sci., 23*, 41, 1975.

Dowden, R. L., Electron energy spectrum and structure deduced from analysis of VLF discrete emissions by using the Helliwell criterion, *J. Geophys. Res., 76*, 3034, 1971*a*.

Dowden, R. L., VLF discrete emissions deduced from Helliwell's theory, *J. Geophys. Res., 76*, 3046, 1971*b*.

Dowden, R. L., A. D. McKay, L. E. S. Amon, H. C. Koons, and M. H. Dazey, Linear and nonlinear amplification in the magnetosphere during a 6.6-kHz transmission, *J. Geophys. Res., 83*, 169, 1978.

Dungey, J. W., Loss of Van Allen electrons due to whistlers, *Planet. Space Sci., 11*, 591, 1963.

Dysthe, K. B., Some studies of triggered whistler emissions, *J. Geophys. Res., 76*, 6915, 1971.

Helliwell, R. A., *Whistlers and Related Ionospheric Phenomena*, Stanford University Press, Stanford, Calif., 1965.

Helliwell, R. A., A theory of discrete VLF emissions from the magnetosphere, *J. Geophys. Res., 72*, 4773, 1967.

Helliwell, R. A., Intensity of discrete VLF emissions, in *Particles and Fields in the Magnetosphere*, edited by B. M. McCormac, p. 292, D. Reidel, Hingman, Mass., 1970.

Helliwell, R. A., Controlled stimulation of VLF emissions from Siple Station, Antarctica, *Radio Sci., 18*, 801, 1983.

Helliwell, R. A., and T. L. Crystal, A feedback model of cyclotron interaction between whistler-mode waves and energetic electrons in the magnetosphere, *J. Geophys. Res., 78*, 7357, 1973.

Helliwell, R. A., and U. S. Inan, VLF wave growth and discrete emission triggering in the magnetosphere: A feedback model, *J. Geophys. Res., 87*, 4427, 1982.

Helliwell, R. A., and J. P. Katsufrakis, VLF wave injection into the magnetosphere from Siple Station, Antarctica, *J. Geophys. Res., 79*, 2511, 1974.

Helliwell, R. A., and J. P. Katsufrakis, Controlled wave-particle interaction experiments, in *Upper Atmosphere Research in Antarctica, Antarctic Res. Ser.*, vol. 29, edited by L. J. Lanzerotti and C. G. Park, pp. 100-129, AGU, Washington, D.C., 1978.

Helliwell, R. A., D. L. Carpenter, and T. R. Miller, Power threshold for growth of coherent VLF signals in the magnetosphere, *J. Geophys. Res., 85*, 3360, 1980.

Helliwell, R. A., U. S. Inan, J. P. Katsufrakis, and D. L. Carpenter, Beat excitation of whistler mode sidebands using the Siple VLF transmitter, *J. Geophys. Res., 91*, 143, 1986*a*.

Helliwell, R. A., D. L. Carpenter, U. S. Inan, and J. P. Katsufrakis, Generation of band-limited VLF noise using the Siple transmitter: A model for magnetospheric hiss, *J. Geophys. Res., 91*, 4381, 1986*b*.

Hess, W. N., *The Radiation Belt and the Magnetosphere*, Blaisdell, Mass., 1968.

Inan, U. S., Nonlinear gyroresonant interactions of energetic particles and coherent VLF waves in the magnetosphere, *Tech. Rep. 3414-3*, Radioscience Lab., Stanford Electronics Labs, Stanford, CA 1977.

Inan, U. S., T. F. Bell, D. L. Carpenter, and R. R. Anderson, Explorer 45 and Imp 6 observations in the magnetosphere of injected waves from the Siple Station VLF transmitter, *J. Geophys. Res., 82*, 1177, 1977.

Inan, U. S., T. F. Bell, and H. C. Chang, Particle precipitation induced by short-duration VLF waves in the magnetosphere, *J. Geophys. Res., 87*, 6243, 1982.

Karpman, V. I., Ja. N. Istomin, and D. R. Shklyar, Nonlinear frequency shift and self-modulation of the quasi-monochromatic whistlers in the inhomogeneous plasma (magnetosphere), *Planet. Space Sci., 22*, 859, 1974*a*.

Karpman, V. I., Ja. N. Istomin, and D. R. Shklyar, Nonlinear theory of a quasi-monochromatic whistler mode wave packet in inhomogeneous plasma, *Plasma Phys., 16*, 685, 1974*b*.

Karpman, V. I., Ja. N. Istomin, and D. R. Shklyar, Effects of nonlinear interaction of monochromatic waves with resonant particles in the inhomogeneous plasma, *Phys. Scr., 11*, 278, 1975.

Kennel, C. F. and Petschek, H. E., Limit on stablely trapped particle fluxes, *J. Geophys. Res., 71* 1, 1966.

Liemohn, H. B., Stimulation of VLF amplification in the magnetosphere, *Space Sci. Rev., 15*, 861, 1974.

Matsumoto, H., Nonlinear whistler-mode interaction and triggered emissions in the magnetosphere: A review, in *Wave Instabilities in Space Plasmas*, edited by P. J. Palmadesso and K. Papadopoulos, p. 163, D. Reidel, Hingham, Mass., 1979.

Matsumoto, H., and Y. Omura, Cluster- and channel-effect phase bunching by whistler waves in a nonuniform geomagnetic field, *J. Geophys. Res., 86*, 779, 1981.

Matsumoto, H., and Y. Omura, Computer simulation studies of VLF triggered emissions: Deformation of distribution function by trapping and detrapping, *Geophys. Res. Lett., 10*, 607, 1983.

Matthews, J. P., Y. Omura, and H. Matsumoto, A study of particle trapping by whistler mode waves in the geomagnetic field: The early development of the VLF quiet band, *J. Geophys. Res., 89*, 2275, 1984.

Murdoch, N., Theory of weakly nonliear VLF interactions, *J. Plasma Phys., 30*, 495, 1983.

Neubert, T., T. F. Bell, and L. R. O. Storey, Resonance between coherent whistler mode waves and electrons in the topside ionospere, *J. Geophys. Res., 92*, 255, 1987.

Nunn, D., A theory of VLF emissions, *Planet. Space Sci., 19*, 1141, 1971.

Nunn, D., A self-consistent theory of triggered VLF emissions, *Planet. Space Sci., 22*, 349, 1974.

Nunn, D., The quasistatic theory of triggered VLF emissions, *Planet. Space Sci., 32*, 325, 1984.

Omura, Y., Study on nonlinear wave-particle interactions in space plasmas via computer simulations, Ph.D. thesis, Kyoto University, Kyoto, Japan, 1985.

Omura, Y., and H. Matsumoto, Computer simulation of basic processes of coherent whistler wave-particle interactions in the magnetosphere, *J. Geophys. Res., 87*, 4435, 1982.

Paschal, E. W., Phase measurements of very low frequency signals from the magnetosphere, Ph.D. thesis, Stanford University, Stanford, California, 1988.

Paschal, E. W., and R. A. Helliwell, Phase measurements of whistler mode signals from the Siple VLF transmitter, *J. Geophys. Res., 89*, 1667, 1984.

Raghuram, R., T. F. Bell, R. A. Helliwell, and J. P. Katsufrakis, Quite band produced by VLF transmitter signals in the magnetosphere, *Geophys. Res. Lett., 4*, 199, 1977.

Ralston, A., and P. Rabinowitz, *A First Course in Numerical Analysis*, McGraw-Hill, New York, p. 191, 1978.

Rastani, K., U. S. Inan, and R. A. Helliwell, DE 1 observations of Siple transmitter signals and associated sidebands, *J. Geophys. Res., 90*, 4128, 1985.

Rathmann, C. E., J. L. Vomvoridis, and J. Denavit, Long-time-scale simulation of resonant particle effects in Langmuir and whistler waves, *J. Comput. Phys., 26*, 408, 1978.

Rietveld, M. T., Monochromatic precursor starts, *J. Geophys. Res., 85*, 2027, 1980.

Rietveld, M. T., R. L. Dowden, and L. E. S. Amon, Micropulsations observed by whistler mode transmissions, *Nature, 276*, 165, 1978.

Roederer, J. G., *Dynamics of Geomagnetically Trapped Particles*, Springer, New York, 1970.

Roux. A., and R. Pellat, A theory of triggered emissions, *J. Geophys. Res., 83*, 1433, 1978.

Stiles, G. S., and R. A. Helliwell, Stimulated growth of coherent VLF waves in the magnetosphere, *J. Geophys. Res., 82*, 523, 1977.

Sudan, R. N., and E. Ott, Theory of triggered VLF emissions, *J. Geophys. Res., 76*, 4463, 1971.

Vomvoridis, J. L., and J. Denavit, Test particle correlation by a whistler wave in a nonuniform magnetic field, *Phys. Fluids, 22*, 367, 1979.

Vomvoridis, J. L., and J. Denavit, Nonlinear evolution of a monochromatic whistler wave in a nonuniform magnetic field, *Phys. Fluids, 23*, 174, 1980.

Vomvoridis, J. L., T. L. Crystal, and J. Denavit, Theory and computer simulations of magnetospheric very low frequency emissions, *J. Geophys. Res., 87*, 1473, 1982.

C. R. Carlson, 340 Velarde St., Mountain View, CA 94041.

R. A. Helliwell, and U. S. Inan, STAR Laboratory, Stanford University, Stanford, CA 94305

(Received February 16, 1988;
revised December 29, 1989;
accepted February 9, 1990.)